Supporting Information:

Nanoscale Surface Structure of Nanometer-Thick Ferroelectric $BaTiO_3$ Films Revealed by Synchrotron X-ray Scanning Tunneling Microscopy: Implications for Catalytic Adsorption Reactions

Pedram Abbasi[1], Nozomi Shirato[2], Rishi E. Kumar[3], Isabel V. Albelo[3], Matthew R. Barone[4], Deniz N. Cakan[1], Ma. de la Paz Cruz-Jáuregui[5], Sarah Wieghold[2], Darrell G. Schlom[4,6,7], Volker Rose[2], Tod A. Pascal[1,3], David P. Fenning*[1,3]*

[1] Department of NanoEngineering, University of California San Diego, La Jolla, CA 92093, USA

[2] Argonne National Laboratory, 9700 S. Cass Avenue, Lemont, IL, 60439, USA

[3] Materials Science and Engineering, University of California, San Diego, La Jolla, USA

[4] Department of Materials Science and Engineering, Cornell University, Ithaca, New York 14853, USA

[5] Centro de Nanociencias y Nanotecnología (CNyN)-Universidad Nacional Autónoma de México (UNAM) Km 107, Carretera Tijuana-Ensenada Ensenada B.C., C.P 22800, Mexico

[6] Kavli Institute at Cornell for Nanoscale Science, Ithaca, New York 14853, USA

[7]Leibniz-Institut für Kristallzüchtung, Max-Born-Str. 2, 12489 Berlin, Germany

Corresponding authors*: tpascal@ucsd.edu (T.A.P), dfenning@eng.ucsd.edu (D.P.F).

Keywords*: Ferroelectrics, X-ray Absorption Spectroscopy, Scanning Tunneling Microscopy, Density Functional Theory, Catalysis*

Material Synthesis:

The $BaTiO_3$ thin films (~15 nm thick) were deposited on (0.5 wt.%) Nb-doped (001)-oriented $SrTiO_3$ substrates (Nb:$SrTiO_3$) by molecular-beam epitaxy (MBE) in a Veeco GEN10 chamber. Prior to growth, the Nb:$SrTiO_3$ substrates were terminated following the procedure developed by Koster *et al*.[1] Elemental barium and titanium were supplied by a conventional effusion cell and a Ti-Ball,[2] respectively. During growth the background pressure was 5×10^{-7} Torr of (O_2 + 10% O_3) and the substrate temperature was 850˚C. Before growth of the $BaTiO_3$ on Nb:$SrTiO_3$, the temperature of the barium source was adjusted until the barium flux incident on the substrate surface matched the titanium flux generated by the Ti-ball[2] operating at 28.0 A. Flux matching was evaluated by monitoring the reflection high energy electron diffraction (RHEED) intensity along the [110] azimuth during shuttered deposition of $BaTiO_3$ on a $GdScO_3$ (110) substrate, akin to the method previously developed for $SrTiO_3$.[3] Once the fluxes of barium and titanium were roughly matched, a 15 nm thick $BaTiO_3$ film was grown on by co-deposition on a (001)-oriented $SrTiO_3$ substrate, and the barium source temperature was adjusted to further optimize the growth condition using surface reconstructions observed with RHEED as feedback. Barium-rich surfaces display a $\sqrt{2}\times\sqrt{2}$ reconstruction (evidenced by ½-order streaks along the [110] azimuth) and require a reduction in the barium source temperature, whereas titanium-rich surfaces display a 2×1 reconstruction (evidenced by ½-order streaks along the [100] azimuth) and warrant an increase in the barium source temperature. Once a recipe was developed for which a 15 nm thick $BaTiO_3$ film could be grown by co-deposition on a (001)-oriented $SrTiO_3$ substrate without displaying any surface reconstruction, final growths were performed by co-deposition on a (001)-oriented Nb:$SrTiO_3$ substrates.

X-Ray Diffraction:

XRD measurements were performed by a Malvern Panalytical Empyrean Diffractometer using Cu K_α x-rays slitted to 0.5˚. When measuring the θ-2θ scan, scattered x-rays were collected in a 0.16 mm slit using a PIXcel3D detector. The reciprocal space map near the 103 peak was collected in a glancing exit geometry, using the PIXcel3D as a 14mm line detector to resolve many scattering angles simultaneously at each step in the scan.

Piezorespone Force Microscopy:

PFM images were taken in an SPM XE-70 from Park Systems, by applying $0.7V_{RMS}$ between the grounded cantilever (ElectricCont-G from BudgetSensors) and the conductive substrate. Polarization reversal was confirmed using the PFM tip to locally apply DC voltages between the grounded tip placed on the film surface, and the bottom conductive $SrTiO_3$:Nb substrate.

To achieve large scale polarization on the ferroelectric surface, the samples were first poled a pristine $BaTiO_3$ film by biasing the surface of the film by +3V, creating a downward polarization across the sample. Next, we attempted to reverse the domain directions written by PFM tip in previous step in a smaller area within the previously poled area (dark rectangles) by applying a bias of -3V. By doing this we confirmed the successful reversal of the domains and ferroelectric switching.

XAS spectroscopy:

The experiments were performed at the XTIP beamline 4-ID-E of the Advanced Photon Source and Center for Nanoscale Materials in Argonne National Laboratory. More details about the specifics of the SX-STM setup can be found in the previous report.[4]

(i) Sample preparation:

A pristine $BaTiO_3$ film was mounted on a Molybdenum sample plate with a back contact. The base pressure of the sample cleaning chamber was 5.0e-10 Torr. The film was cleaned with multiple cycles of Ar^+ sputtering (3.0 μA, 1.0 kV) for 20 minutes, followed by annealing at 530 C for 30 minutes under oxygen dosing (7.5e-6 Torr) and final annealing at 640 C for 10 minutes. Following the sample cleaning, the film was transferred to the SX-STM analysis chamber with a vacuum suitcase maintaining UHV condition (1e-10 Torr).

(ii) XAS Spectroscopy on Bare Surfaces:

To perform *tunneling regime* X-ray absorption spectroscopy (XAS), first, a smart tip (coaxial STM tip) apex was positioned a few nm away from a surface outside of the tunneling regime in order to detect photo-ejected electrons from the sample. A focused monochromatic X-ray beam (size of ~10x10 μm) is aligned to the tip-sample junction. Next, the tip is brought into tunneling. A tunneling current setpoint and a sample bias were set at 100pA and +0.1V, respectively. While the tip is maintaining tunneling condition, X-ray beam the energy was changed from 778.5 to 803.5eV, 525 to 545eV and 453.5 to 468.5eV with a step size of 0.1eV to probe Ba *M*, O *K* and Ti *L* edges, respectively. For single-point spectroscopic data presented in Figure 2, three spectra at each pre-biased area were measured and the average response was calculated.

(iii) In-situ sample biasing:

For in-situ biasing experiments, the tip was retracted by 2 nm. This brings the tip out of the tunneling regime. The sample voltage was ramped up to a poling bias (i.e. +10V) and was maintained for 10 minutes to ensure poling saturation of the ferroelectric film. Once the poling was completed, the tip moved back to tunneling condition with I=100pA and V=+0.1V.

(iv) Gas dosing

Oxygen was dosed in the SX-STM chamber from an oxygen gas cylinder (99.999%, Airgas) using a precision leak valve. Following a sample poling with a tip on the $BaTiO_3$ film, oxygen was dosed to the chamber at $2.5e^{-6}$ Torr for 10 minutes. During the dosing, the X-ray beam was turned off and the sample was kept at room temperature. Once dosing was completed, we immediately closed the leak valve and a turbo molecular pump removed residual gas from the chamber.

(v) *Chemical mapping*

Mapping was achieved by scanning the sample surface while the X-ray beam illuminates the tip-sample junction at an elemental edge peak energy (i.e., Ti *L* edge peak, 456.5eV). The X-ray beam is modulated by an ultra-high vacuum optical chopper at 650 Hz, creating beam ON and OFF states at the tip-sample junction. By utilizing a lock-in amplifier as well as an FPGA-based real time signal filter, we separated the tip signal into two channels; beam "OFF" channel for the STM topological feedback, and the beam "ON" channel for X-ray induced chemical signals. Local elemental and chemical state variations appear as an image contrast. Hence, this enables collecting topography and chemical information together while examining the sample surface. Here, in X-ray mapping mode we set the tunneling current to 100 pA, sample bias to +0.1 V, and scanning speed to 40 msec/pixel. Chemical mapping was performed on an area of

~80×95nm^2 with ~100x120 pixels on Ti *L*, O *K* and Ba *M* edges under two polarization states. To understand the net chemical intensity of each signal, we normalized the XAS intensity of each pixel to its intensity at the reference pre-edge energy. (Eq. S1) The main edge and pre-edge energy values were chosen to maximize the contrast between two polarization states. [See Figure S6 for an example]. We performed elemental mapping for energies above and below each elemental edge (i.e., Ti *L*, Ba *M* and O *K*) under upward and downward polarization, for a total of 12 maps (Figure S7). Moreover, to rule out topographical effects, we subtracted the STM dark current (beam "OFF") from total X-Ray induced tunneling current (beam "ON") to only consider chemical shifts at the surface upon polarization switching. (Eq. S2). We then created contrast maps based on the difference between the intensity of each pixel at its upward and downward polarized states (Eq. S3) The details of steps we took are as follows:

The total tunneling current in SX-STM measurements is the sum of both STM tunneling current, X-ray excited photoelectrons.

$$\mathbf{I_{SX\text{-}STM}} = \mathbf{I}_{tunneling\ (dark)} + \mathbf{I}_{tunneling\ (X\text{-}ray)} \quad (S1)$$

Where $\mathbf{I_{tunneling(dark)}}$ is the conventional tunneling current controlled by a feedback loop, and $\mathbf{I_{tunneling\ (X\text{-}ray)}}$ is the X-ray excited/enhanced tunneling current generated from tunneling electrons of the tip-surface area being boosted by X-ray irradiation under the tip.

For dark (beam-off) maps shown as $\mathbf{I_{tunneling}}$ **(Dark)** intensities and contrast maps were calculated based on the following steps:

$$\mathbf{I}_{norm\ (dark)} = I_{(edge)} / I_{(pre\text{-}edge)} \quad (S2)$$

$$\Delta\mathbf{I}_{net_{(dark)}} = I_{norm\_dark}(\text{up}) - I_{norm\_dark}(\text{down}) \quad (S3)$$

For chemical maps shown as $\mathbf{I}_{\mathbf{tunneling}}$ **(X-Ray)** intensities and contrast maps were calculated based on the following steps:

$$\mathbf{I}_{chemical} = I(\textit{Beam "ON"}) - I(\textit{Beam "OFF"}) \qquad (S4)$$

$$\mathbf{I}_{norm\_chemical} = I_{chemical\ (edge)} / I_{chemical\ (pre\text{-}edge)} \quad (S5)$$

$$\Delta\mathbf{I}_{chemical\ net} = I_{norm\_chemical}\ (\text{up}) - I_{norm\_chemical}\ (\text{down}) \quad (S6)$$

DFT calculations:

DFT calculations were performed with the Quantum ESPRESSO package.[5] Typical unit cells comprised 6 layers $BaTiO_3$ on 3 layers of Pt acting as a charge reservoir. To accurately mimic the surface of a thick film, the first two layers of $BaTiO_3$ in contact with the Pt electron reservoir were fixed at their bulk ferroelectric coordinates, while the top 4 layers were allowed to fully relax along with adsorbates until the residual forces on the atoms were smaller than a 0.01eV/Å threshold. We used a ~10Å thick vacuum on each side of the slabs in addition to dipole corrections to prevent spurious interactions between the opposite surfaces. To treat the on-site coulombic interaction of the Ti d localized electrons, we implemented the GGA+U approximation, with a U = 4 eV term, which was previously shown to be effective in correcting artifacts arising from the conventional GGA method in electronic structure calculations.[6]

We further investigated the binding energy of O_2 molecules on (001) $BaTiO_3$ surfaces with two different terminations: BaO and TiO_2, with upward and downward polarization. (Figure S5) Free energy of adsorption for O_2* on each polarized slabs were calculated using the following equation:

$$\Delta G_{H^*} = \Delta E + \Delta ZPE - T\Delta S$$

Other details of calculations are similar to our previous work.[7] For this study the ZPE and $T\Delta S$ were 0.10 and 0.64 respectively, as obtained from Ref [8].

Computational XAS calculations:

Near-edge X-ray absorption spectroscopy relies on excitation of core-level electrons to unoccupied, conduction band states. Most computational approaches for simulating XAS is based on application of Fermi's Golden Rule.[9,10] While our previous work[11] implemented a computationally efficient, delta self-consistent field (ΔSCF) [10,12] for generating the spectrum, here we employ the Bethe-Salpeter equation, since capturing the effect of lattice distortion at atomic scale and spin-orbit coupling[13] on transition metals involves multiple many-electron effects that are absent in ΔSCF approaches. The BSE method includes both a screened, direct attraction between the excited electron and hole and an unscreened repulsive exchange term,[13] making it a reliable tool in computing XAS response in O *K* and transition metals *K* and *L* edges in metal oxides and pervoskites.[14–17] However, computational XAS investigation of transition metal *M*-edges usually requires other techniques that are particularly developed for strongly correlated systems.[18] Based on this consideration, here we do not investigate the BSE results of Ba *M* edge for our polarized models computationally. All our XAS calculations were performed using the OCEAN 2.9.7 code.[15] For these calculations we used a 1x1x5 slab with ~15A of vacuum at each side. A 2x2x2 k-point grid was used for the SCF calculations. To represent the upward and downward polarization states (and thus breaking the symmetry across the slab model), the topmost layer was distorted based on experimental values for upward and downward polarization (see Figure S3). All density-functional-theory (DFT) calculations were performed with the Quantum ESPRESSO package,[5] with the exchange-correlation energies approximated using the Local

density approximation (LDA). Norm-conserving pseudopotentials from the pseudo-dojo[19] distribution were used, with a cutoff energy of 80 Ry. The size of the k-point grid used to solve the Kohn–Sham DFT states for BSE was 2 × 2 × 2.

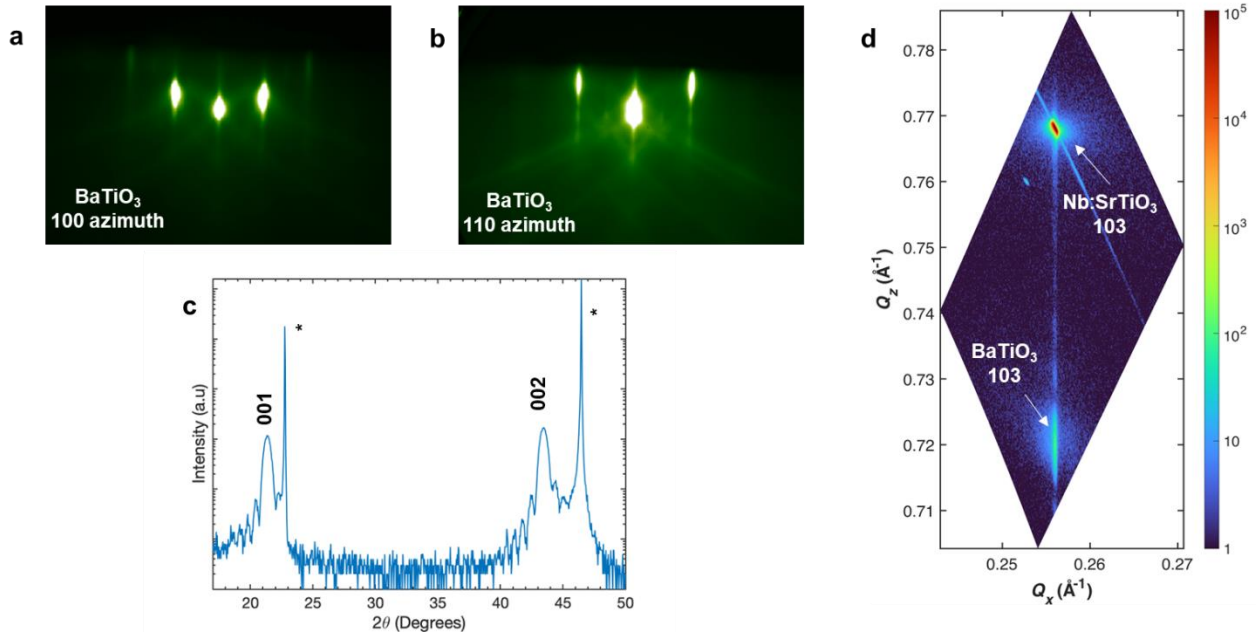

Figure S1. Structural characteristics of the (001)-oriented $BaTiO_3$ films on Nb:$SrTiO_3$; (a-b) RHEED pattern of $BaTiO_3$ films viewed along the [110] and [100] azimuth; (c) XRD θ-2θ scans of $BaTiO_3$ films (substrate peaks are denoted by an asterisk "*") (d) RSM map of epitaxial $BaTiO_3$/Nb: $SrTiO_3$ film showing the 103 reflections of both film and substrate.

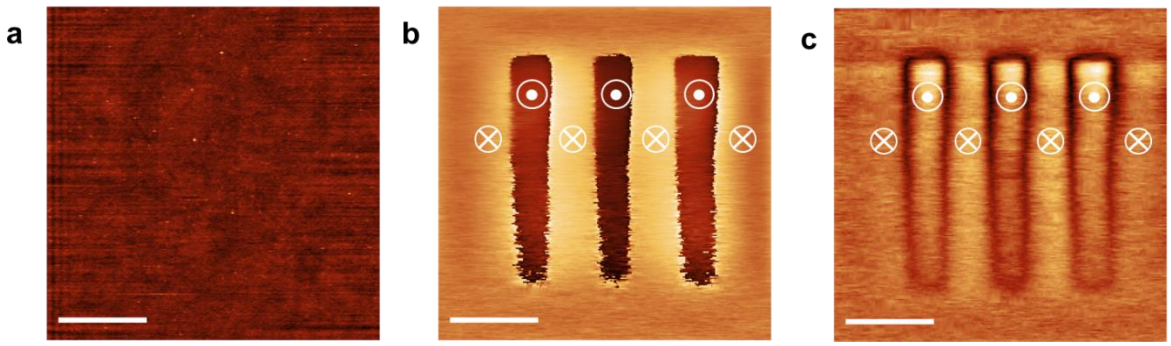

Figure S2. (a) Topography, with a RMS roughness (R_q) of *1.8* Å; (b) Phase and (c) amplitude PFM images after the as grown sample was poled downward with +3Vand then re-poled upward (dark brown zones in (b)) with -3V, applied between the bottom electrode and the grounded PFM tip. Scale bars are 2 µm.

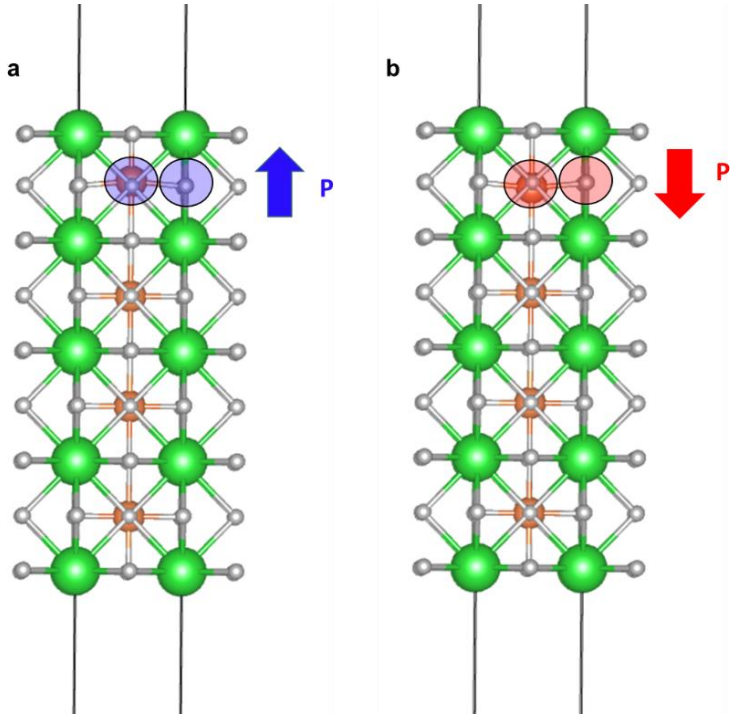

Figure S3. Snapshots of the slabs used for BSE XAS calculations (a) slab with upward local polarization; (b) with downward local polarization near the surface. Ba, Ti, and O atoms are shown with green, orange and gray spheres, respectively. Excited Ti and O atoms are highlighted.

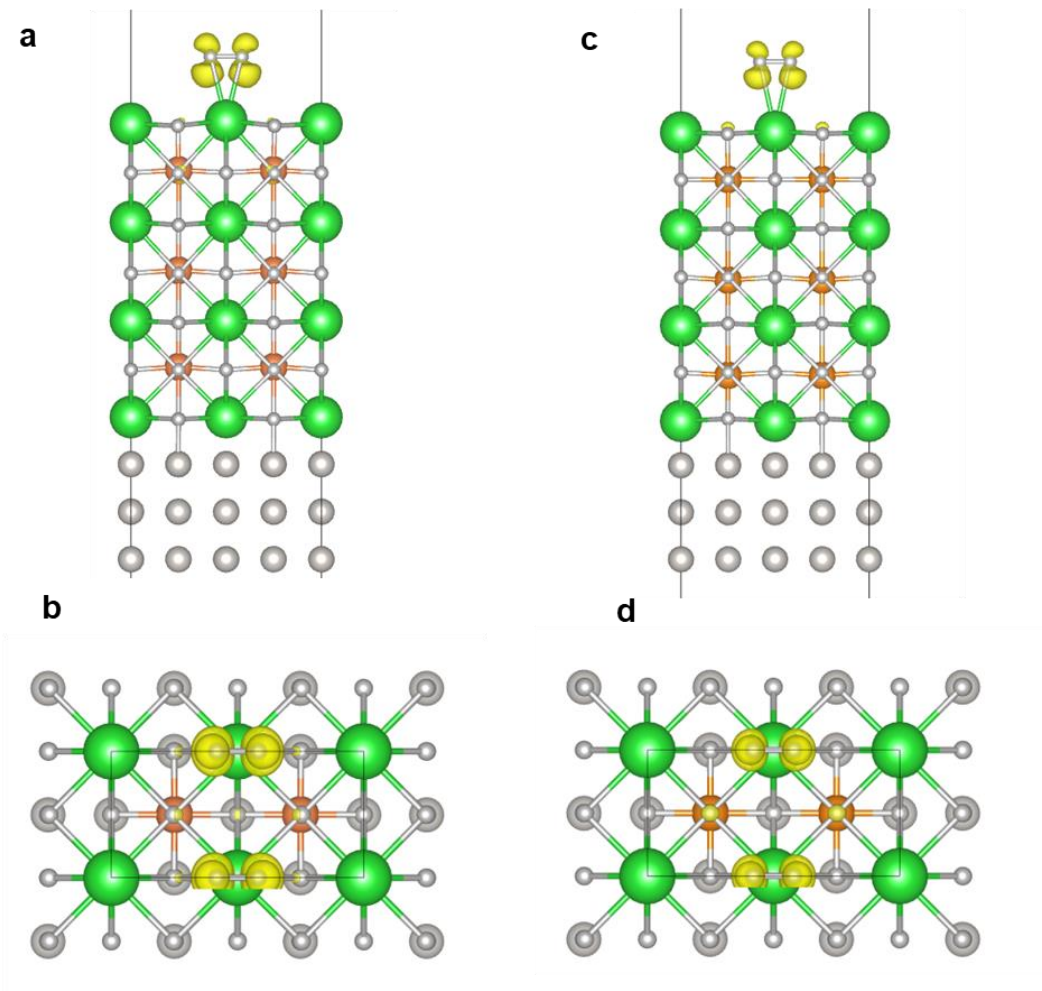

Figure S4. Snapshots of relaxed structures of (001) BaO-terminated slabs with O_2* molecule adsorbed on Ba sites exhibiting electron difference after O_2 adsorption of (a,b) poled up and (c,d) poled down models. Ba, Ti, O, and H are shown with green, orange, gray, and white spheres, respectively.

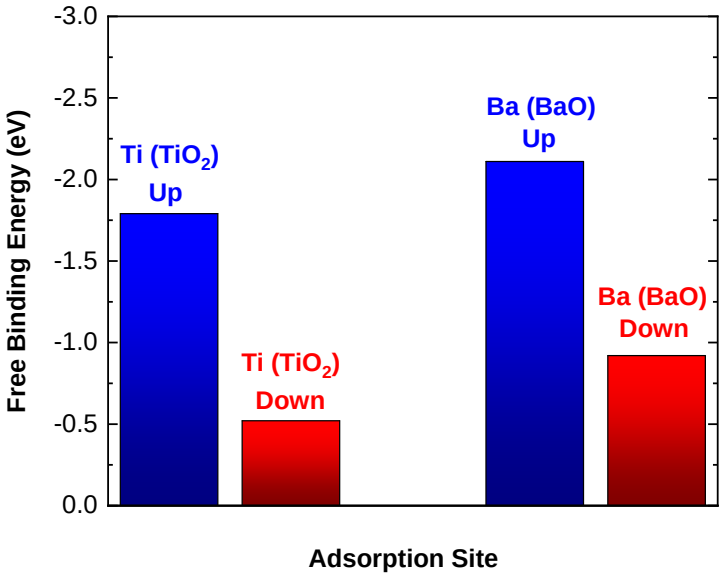

Figure S5. Binding free energy of O_2 adsorption on (a) O site and (b) metal of BaO and TiO_2 terminated (001) $BaTiO_3$ slabs with upward (blue) and downward (red) polarization.

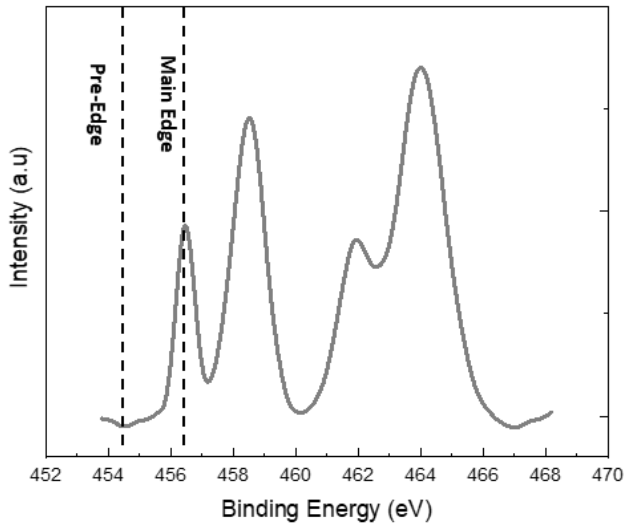

Figure S6. Position of pre-edge and main edge energy identified on example Ti *L* edge.

Table S1.Position of pre-edge and main edge energies on Ti *L*, O *K* and Ba *M* edges.

Scan	Energy (eV)
Ti ***L*** (Pre-Edge)	454.5
Ti ***L*** (Main-Edge)	456.5
Ba ***M***(Pre-Edge)	781.0
Ba M(Main-Edge)	783.4
O ***K*** (Pre-Edge)	526.0
O ***K*** (Main-Edge)	529.1

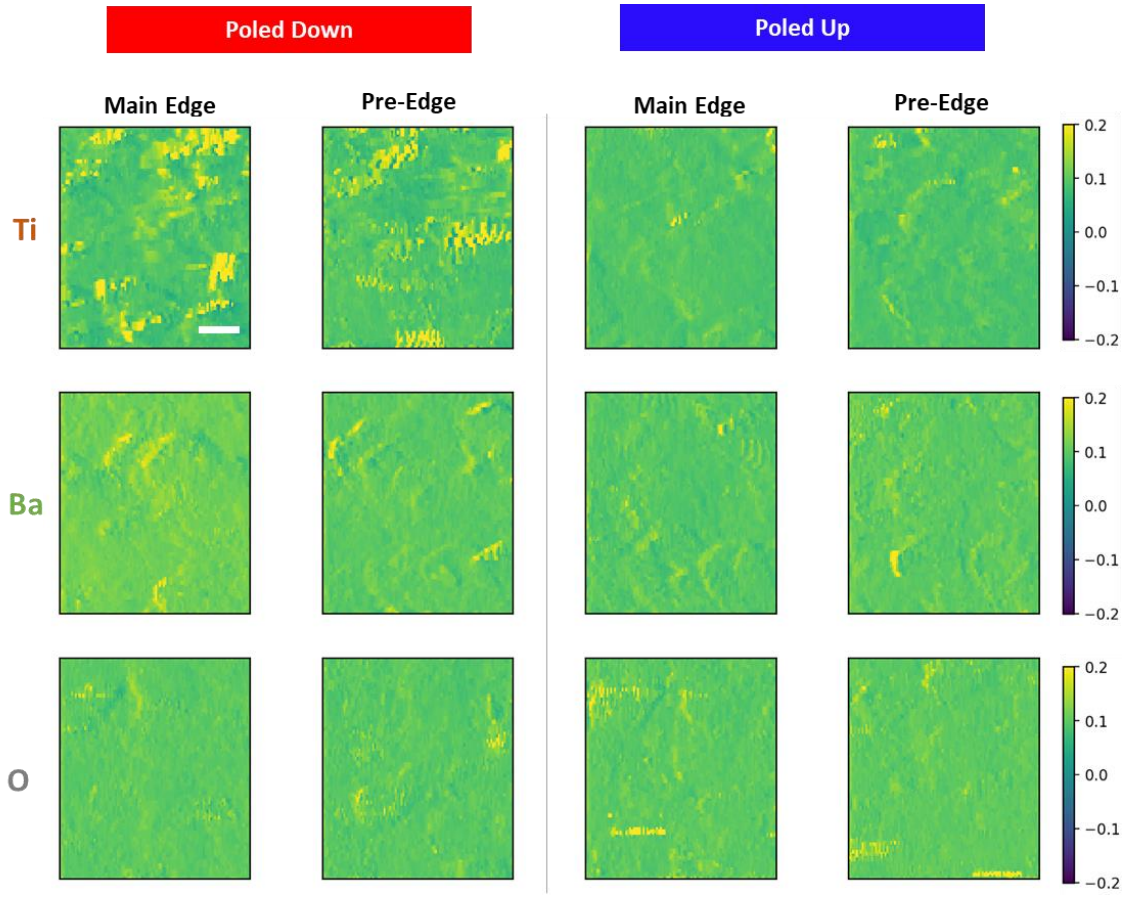

Figure S7. Elemental maps taken at main edge and pre-edge positions of Ti *L*, Ba *M* and O *K* edges for samples with upward and downward polarization under X-ray illumination. Scale bar is 15nm.

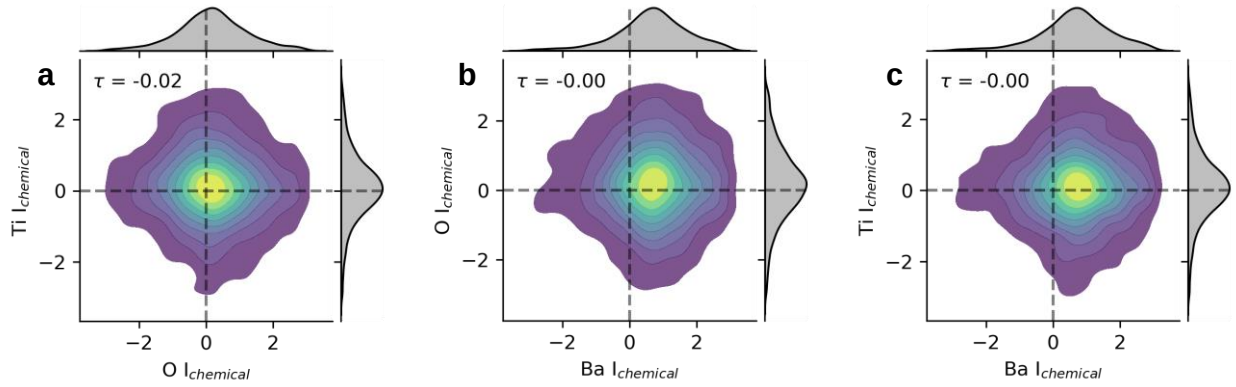

Figure S8: **Density plots of coincident chemical signals** (a)Ti vs O (b) O vs Ba and (c) Ti vs Ba. The marginal plots show the distribution of each individual chemical signal Dotted lines demarcate values of 0. The value in the upper left-hand corner is the Kendall rank correlation coefficient between the two signals. The individual chemical signals are taken from Figure 5g' – i' in the main text.

References:

(1) Koster, G.; Kropman, B. L.; Rijnders, G. J. H. M.; Blank, D. H. A.; Rogalla, H. Quasi-Ideal Strontium Titanate Crystal Surfaces through Formation of Strontium Hydroxide. *Appl. Phys. Lett.* **1998**, *73* (20), 2920–2922. https://doi.org/10.1063/1.122630.

(2) Theis, C. D.; Schlom, D. G. Cheap and Stable Titanium Source for Use in Oxide Molecular Beam Epitaxy Systems. *J. Vac. Sci. Technol. A Vacuum, Surfaces, Film.* **1996**, *14* (4), 2677–2679. https://doi.org/10.1116/1.580185.

(3) Haeni, J. H.; Theis, C. D.; Schlom, D. G. RHEED Intensity Oscillations for the Stoichiometric Growth of SrTiO3 Thin Films by Reactive Molecular Beam Epitaxy. *J. Electroceramics* **2000**, *4* (2), 385–391. https://doi.org/10.1023/A:1009947517710.

(4) Rose, V.; Ajayi, T.; Rosenmann, D.; Shirato, N. A Variable X-Ray Chopper System for Phase-Sensitive Detection in Synchrotron X-Ray Scanning Tunneling Microscopy. *J. Synchrotron Radiat.* **2020**, *27* (5), 1382–1387. https://doi.org/10.1107/S1600577520007869.

(5) Giannozzi, P.; Baroni, S.; Bonini, N.; Calandra, M.; Car, R.; Cavazzoni, C.; Ceresoli, D.; Chiarotti, G. L.; Cococcioni, M.; Dabo, I.; Dal Corso, A.; De Gironcoli, S.; Fabris, S.; Fratesi, G.; Gebauer, R.; Gerstmann, U.; Gougoussis, C.; Kokalj, A.; Lazzeri, M.; Martin-Samos, L.; Marzari, N.; Mauri, F.; Mazzarello, R.; Paolini, S.; Pasquarello, A.; Paulatto, L.; Sbraccia, C.; Scandolo, S.; Sclauzero, G.; Seitsonen, A. P.; Smogunov, A.; Umari, P.; Wentzcovitch, R. M. QUANTUM ESPRESSO: A Modular and Open-Source Software Project for Quantum Simulations of Materials. *J. Phys. Condens. Matter* **2009**. https://doi.org/10.1088/0953-8984/21/39/395502.

(6) Ali, A.; Khan, I.; Ali, Z.; Khan, F.; Ahmad, I. First-Principles Study of BiFeO 3 and BaTiO 3 in Tetragonal Structure. *Int. J. Mod. Phys. B* **2019**, *33* (21), 1950231. https://doi.org/10.1142/S021797921950231X.

(7) Abbasi, P.; Barone, M. R.; de la Paz Cruz-Jáuregui, M.; Valdespino-Padilla, D.; Paik, H.; Kim, T.; Kornblum, L.; Schlom, D. G.; Pascal, T. A.; Fenning, D. P. Ferroelectric Modulation of Surface Electronic States in BaTiO 3 for Enhanced Hydrogen Evolution Activity. *Nano Lett.* **2022**, *22*

(10), 4276–4284. https://doi.org/10.1021/acs.nanolett.2c00047.

(8) Valdés, Á.; Qu, Z. W.; Kroes, G. J.; Rossmeisl, J.; Nørskov, J. K. Oxidation and Photo-Oxidation of Water on TiO2 Surface. *J. Phys. Chem. C* **2008**, *112* (26), 9872–9879. https://doi.org/10.1021/jp711929d.

(9) Henderson, G. S.; Groot, F. M. F. De; Moulton, B. J. A. X-Ray Absorption Near-Edge Structure (XANES) Spectroscopy. **2014**, *78*, 75–138.

(10) Liang, Y.; Vinson, J.; Pemmaraju, S.; Drisdell, W. S.; Shirley, E. L.; Prendergast, D. Accurate X-Ray Spectral Predictions: An Advanced Self-Consistent-Field Approach Inspired by Many-Body Perturbation Theory. *Phys. Rev. Lett.* **2017**, *118* (9). https://doi.org/10.1103/PhysRevLett.118.096402.

(11) Shirato, N.; Cummings, M.; Kersell, H.; Li, Y.; Stripe, B.; Rosenmann, D.; Hla, S.-W.; Rose, V. Elemental Fingerprinting of Materials with Sensitivity at the Atomic Limit. *Nano Lett.* **2014**, *14* (11), 6499–6504. https://doi.org/10.1021/nl5030613.

(12) Ljungberg, M. P.; Mortensen, J. J.; Pettersson, L. G. M. An Implementation of Core Level Spectroscopies in a Real Space Projector Augmented Wave Density Functional Theory Code. *J. Electron Spectros. Relat. Phenomena* **2011**, *184* (8–10), 427–439. https://doi.org/10.1016/j.elspec.2011.05.004.

(13) Lee, M. C.; Lee, S.; Won, C. J.; Lee, K. D.; Hur, N.; Chen, J. L.; Cho, D. Y.; Noh, T. W. Hybridized Orbital States in Spin-Orbit Coupled 3d-5d Double Perovskites Studied by x-Ray Absorption Spectroscopy. *Phys. Rev. B* **2018**, *97* (12), 125123. https://doi.org/10.1103/PhysRevB.97.125123.

(14) Li, L.; Lee, E.; Freeland, J. W.; Fister, T. T.; Thackeray, M. M.; Chan, M. K. Y. Identifying the Chemical Origin of Oxygen Redox Activity in Li-Rich Anti-Fluorite Lithium Iron Oxide by Experimental and Theoretical X-Ray Absorption Spectroscopy. *J. Phys. Chem. Lett.* **2019**. https://doi.org/10.1021/acs.jpclett.8b03271.

(15) Vinson, J.; Rehr, J. J.; Kas, J. J.; Shirley, E. L. Bethe-Salpeter Equation Calculations of Core Excitation Spectra. *Phys. Rev. B - Condens. Matter Mater. Phys.* **2011**. https://doi.org/10.1103/PhysRevB.83.115106.

(16) Gilmore, K.; Vinson, J.; Shirley, E. L.; Prendergast, D.; Pemmaraju, C. D.; Kas, J. J.; Vila, F. D.; Rehr, J. J. Efficient Implementation of Core-Excitation Bethe-Salpeter Equation Calculations. *Comput. Phys. Commun.* **2015**, *197* (November), 109–117. https://doi.org/10.1016/j.cpc.2015.08.014.

(17) Rehr, J. J. Theory and Calculations of X-Ray Spectra: XAS, XES, XRS, and NRIXS. *Radiat. Phys. Chem.* **2006**. https://doi.org/10.1016/j.radphyschem.2005.11.014.

(18) Jia, C. A Wannier Orbital Based Method for Resonant Inelastic X-Ray Scattering Simulation. *J. Phys. Conf. Ser.* **2019**, *1290* (1). https://doi.org/10.1088/1742-6596/1290/1/012014.

(19) van Setten, M. J.; Giantomassi, M.; Bousquet, E.; Verstraete, M. J.; Hamann, D. R.; Gonze, X.; Rignanese, G.-M. The PseudoDojo: Training and Grading a 85 Element Optimized Norm-Conserving Pseudopotential Table. *Comput. Phys. Commun.* **2018**, *226*, 39–54. https://doi.org/10.1016/j.cpc.2018.01.012.